



Fiber orientation measurement from mesoscale CT scans of prepreg platelet molded composites

Benjamin R. Denos^{a,*}, Drew E. Sommer^a, Anthony J. Favaloro^a, R. Byron Pipes^a, William B. Avery^b

^a *Purdue University, Composites Manufacturing and Simulation Center, Indiana Manufacturing Institute, 1105 Challenger Avenue, Suite 100, West Lafayette, IN 47906, United States*

^b *Boeing Commercial Airplanes, Seattle, WA, United States*

ARTICLE INFO

Keywords:

- A. Prepreg
- B. Directional orientation
- D. CT analysis
- E. Compression moulding

ABSTRACT

X-ray computed tomography (CT) analysis is used to measure the heterogeneous fiber orientation fields in a 20 cm³ composite bracket made from prepreg platelet-based molding compound (PPMC). The as-molded mesostructure of the complete geometry is captured using material density gradients in 50 μm resolution CT scans without the need to resolve individual fibers. Fiber collimation and physical density gradients within intact platelets of this material system facilitates nondestructive assessment of average local fiber orientation at the component scale. Microscopy-based validation of the local orientation measurements indicate the accuracy that can be attained utilizing the density-based structure tensor CT analysis method. Local orientation field measurements for the complete geometry can be mapped into a “digital twin” model, for purposes such as experimental performance simulation and validation of molding process orientation state predictions. Composite designers, analysts, and material suppliers can employ this methodology to more confidently utilize PPMCs and morphologically similar composite material systems.

1. Introduction

Prepreg platelet molding compound (PPMC) material systems fill a niche between high volume, low performance short fiber reinforced injection molded materials and continuous fiber reinforced materials [1]. Platelets can be cut directly from continuous woven materials, unidirectional tape or continuous fiber tows [2,3]. The present work focuses on carbon fiber reinforced thermoplastic platelets cut from prepreg, unidirectional tape where aligned fibers of high volume fraction are inherited from the parent material, enhancing mechanical performance over short fiber systems. Platelets may be part of a highly ordered system [4] or, more commonly, deposited with an uncontrolled orientation state to form a stochastic morphology [5] as with the geometry presented.

The discontinuous nature of the free platelets in the PPMC assembly allows deformation and flow to fill complex geometries not readily achievable with continuous fiber composites. Final orientation state is a function of both initial orientation state and induced orientation changes due to material deformation during molding. Just as orientation state is critical to determine mechanical behavior of traditional laminated composites, determining the platelet orientation field is

necessary to characterize anisotropic mechanical behavior in PPMC material systems.

Microscopy is commonly used to accurately, but destructively, determine the microstructural and mesostructural details within fiber-based composite material systems [6]. Inspection of high magnification micrographs can clearly show individual fibers [7], tows [8–10], voids [11], damage [12,13], and other microstructural details. For cylindrical fibers, orientation can be determined from exposed elliptical cross-sections. There are few methods as accessible and accurate as microscopy for characterizing the microstructure of composite materials, but the method is destructive and inspected regions are typically small when compared to part geometry.

Micrometer scale computed tomography, or micro CT, can be an accurate method for nondestructive inspection of small material volumes to show details of fibers, tows [8,14,15], voids [16–18], and damage [19,20] in both long and short fiber composites. Micro- or nanometer scan resolutions allow individual fibers to be distinguished for short fiber [21,22], uncontrolled long fiber [23,24] and laminated material systems [25–29]. With clearly discernable fibers or tows, commercially available software such as Volume Graphics VGStudio MAX can be used to determine fiber orientation [22,30,31] and for

* Corresponding author.

E-mail address: bdenos@purdue.edu (B.R. Denos).

<https://doi.org/10.1016/j.compositesa.2018.08.024>

Received 2 April 2018; Received in revised form 17 August 2018; Accepted 18 August 2018

Available online 20 August 2018

1359-835X/ © 2018 Elsevier Ltd. All rights reserved.

porosity segmentation analysis [17] of the CT volume. However, as sample size increases, the CT resolution decreases, thereby making it difficult or impossible to discern fiber-scale details. Procedures exist to manipulate the scanning setup and reconstruction software to allow for larger scan volumes while retaining mesoscale resolution required for extension of the methodology in this work [32,33], but a traditional CT scan is used for the presented results.

The individual tools required to facilitate large scale CT fiber orientation analysis have been available previously, but have not been combined for the scale and material system in this work. In fact, the scan resolution of the $100 \times 100 \times 25$ mm “T-Shapes” in the work of Leblanc [34] is appropriate for this method and the image analysis methodology of Krause [35] is very similar to this work, but was applied at the fiber scale. Han performed a workflow similar to this paper using VGStudio MAX orientation analysis as the baseline for validation of Moldflow simulation with a similar material system, but did not validate the CT-based orientations with microscopy-based orientation measurements [36,37].

While micro CT and microscopy provide excellent local fiber orientation measurement for detailed inspection and validation purposes, local microstructure in PPMCs should not be extrapolated to represent the microstructure throughout such a morphologically heterogeneous material system. A methodology is presented to utilize mesoscale $50 \mu\text{m}$ resolution CT scans of complete 19cm^3 specimens with an understanding that the compression-molded geometry inspected has a mesostructure of platelets consisting of locally aligned fibers. This mesostructure enables the connection of the in-situ platelet density state and orientation fields. Nondestructively obtaining orientation state data at a resolution that is both sufficient and useful for part-scale analysis is an improvement over other laborious and spatially limited microscopic analysis methods.

2. Experimental materials and methods

2.1. Compression molding uncontrolled platelet charges

The parent material of the platelet system investigated is a commercially available, pre-impregnated unidirectional tape containing 50–60% carbon fiber by volume and a thermoplastic matrix. This tape is cut to 12.7 mm lengths and slit to various widths as desired. The platelet thickness is approximately 0.15 mm, and is the same as the parent tape. The bulk PPMC of loose platelets is weighed and poured into the charge cavity of the steel tool in Fig. 1. A ramhead is placed above the material in the charge cavity, and the tool and material are raised above the thermoplastic polymer melt temperature. Once the target temperature is achieved, the tool is transferred to a hydraulic press that applies an effective pressure from the ramhead to the material charge. The melted bulk material flows into the net-shape tool cavity and consolidates under load. The tool is cooled well below the matrix melt temperature, disassembled and the part is extracted. CT scanning and then microscopy are used to investigate the molding-

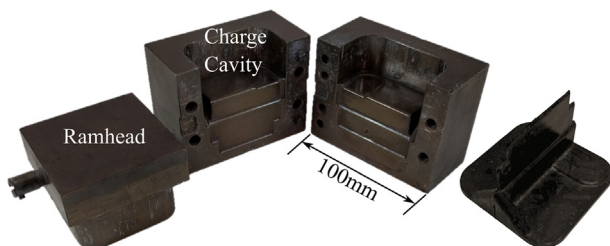


Fig. 1. T bracket compression molding tool and specimen. (For interpretation of the references to colour in this figure legend, the reader is referred to the web version of this article.)

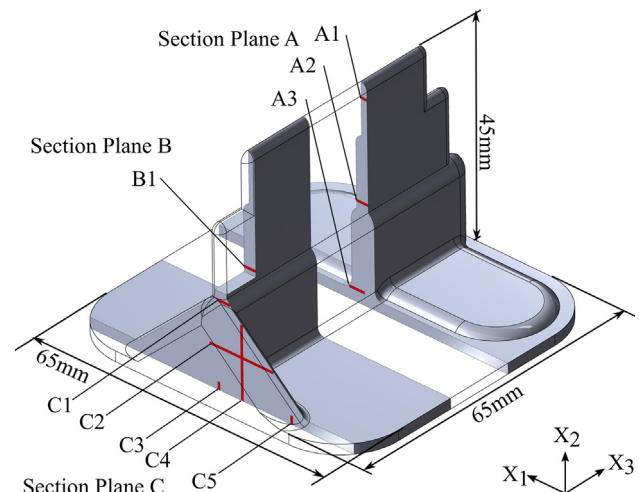


Fig. 2. Inspection planes and lines (in red) for microscopy and CT analysis comparison. (For interpretation of the references to colour in this figure legend, the reader is referred to the web version of this article.)

induced microstructure with fiber orientation field in the finished part as the primary goal.

2.2. Microscopy to inspect molding induced microstructure

Optical microscopy with bright-field lighting was employed to determine the baseline fiber orientation measurement of micro- and mesostructure for the PPMC. After CT scanning is performed, three section planes of interest are chosen such that each will contain regions of unique flow-induced orientation states near the charge cavity and in planar regions of varying thickness. These section planes and specific inspection lines are seen in Fig. 2. A thin diamond-grit sectioning blade is used to perform the cuts precisely and leave external specimen boundaries intact wherever possible as references for spatial location of the regions of interest within the part. The specimen sections are then mounted in epoxy to facilitate polishing. A grinding and polishing procedure for carbon fiber-reinforced polymers is then performed until the inspection planes show individual sectioned fiber ellipses clearly. The polished specimen sections are placed on an inverted optical microscope and images of the inspection regions are taken at $200\times$ magnification and stitched together into a detailed mosaic with image acquisition software. The image resolution is then ideal for detailed local microstructure characterization.

A visual inspection of the mosaic images shows the mesostructure of the part without image analysis. Observations demonstrate that where part geometry is thin (approximately 1–5 mm) and planar, platelets tend to align parallel to surface boundary planes. An example of the laminated platelet structure with intact platelets can be seen in the stitched micrographs of Fig. 3, where surface boundaries are seen on either side and individual fiber cross-sections appear as light gray ellipsoids. The resolution difference between a micrograph and a single slice of CT scan data at the same location is also seen in Fig. 3, where each voxel appears as a $53 \times 53 \mu\text{m}$ pixel, and gray values correspond to X-ray attenuation through different local densities. Thick regions or those where more complex material flow occurs sufficiently far from tool boundaries may contain fully 3D platelet orientations as shown in the middle right of Section Plane C in Fig. 4.

2.3. Micrograph fiber orientation measurement

Fiber ellipse cross sections in digital micrographs provide enough data to determine the fiber orientation angle, ϕ , from the X_1 toward the X_2 axis (within the section plane) and angle θ from the $+X_3$ axis toward

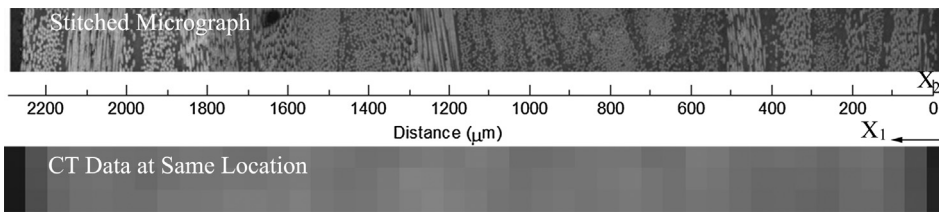


Fig. 3. Microscopy and CT data example at location A2. (For interpretation of the references to colour in this figure legend, the reader is referred to the web version of this article.)

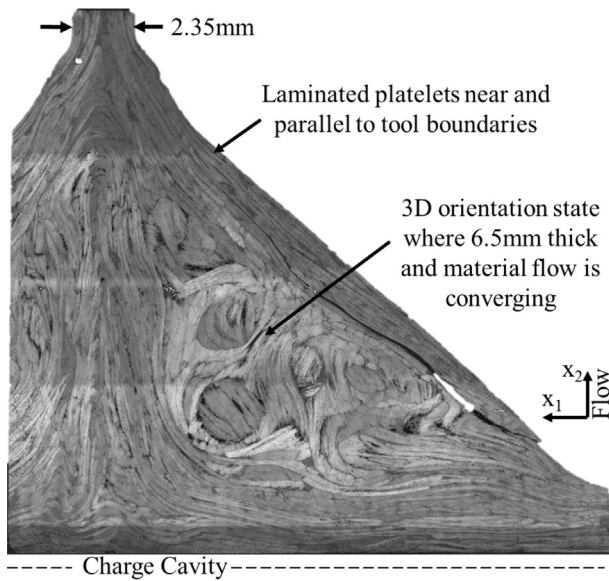


Fig. 4. Section plane C stitched micrographs.

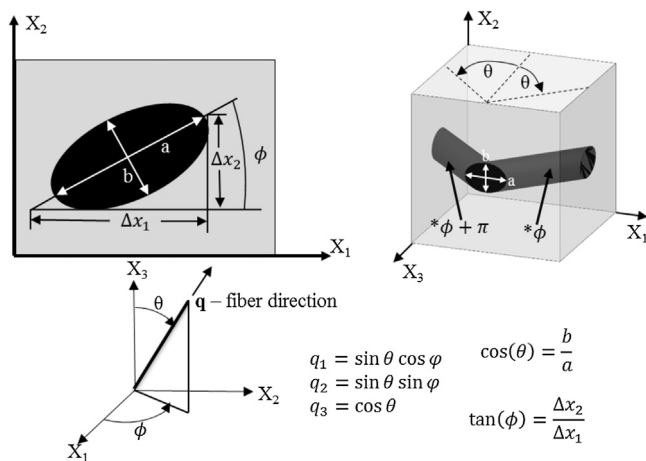


Fig. 5. Fiber orientation definition from fiber ellipse cross sections.

the X_1 - X_2 plane for each measured fiber according to Fig. 5. For the micrograph image analysis method used, angle θ is bounded as $[0, \frac{\pi}{2}]$, but ϕ may actually be $\phi \pm \pi$, representing an alternate fiber orientation having the same ellipse shown in Fig. 5 [38]. Angle ϕ remains ambiguous without serial sectioning, confocal imaging, or another method to determine which of the two directions is correct [39]. The fiber orientation vector components q_i from microscopy measurement are derived from θ and ϕ and used as the primary orientation definition because they are more spatially intuitive within a Cartesian global coordinate system. CT orientation vector P and its components, P_i , are reserved for the definition of CT-based orientation vector measurements.

Local fiber collimation within the platelet allows for local orientation definition by a single fiber vector. Fiber cross section ellipse-based

θ and ϕ measurements are taken in each platelet, or aligned fiber bundle region, at fibers every $20 \mu\text{m}$ or less along the centerline of each stitched micrograph to capture large inter- and small intra-platelet orientation changes. The digital micrographs are opened in Fiji and the ellipse region of interest tool is used to outline the selected fibers prior to selecting “measure” to obtain each ellipse major and minor axis and the angle from horizontal to major axis [40]. With a fiber diameter of 55 pixels for the $7 \mu\text{m}$ diameter fibers, there is potential for an 11° measurement error when the fiber cross sections are nearly circular according to the measured geometry explanations by Bay and Tucker [7]. The determined fiber orientation vectors are not averaged in any way so that both intra- and inter-platelet orientation variability can be seen point-by-point in the plotted results used for comparison with CT measurements.

The microscopy-measured orientation state may exhibit abrupt transitions, so it is critical to compare data at the correct location in the CT-measured data. A positional mismatch as small as a single platelet thickness during comparison may offset all orientation comparisons and result in an apparent failure of the CT measurement method. Physical measurements of polished specimen plane locations within the overall geometry and identification of unique microstructures visible in micrographs and CT slices are used to correctly register the two datasets for final comparison. The microscopy-based data provides an accurate baseline of local fiber orientation for comparison with the CT scan analysis orientation data.

2.4. CT scans of parts

CT scans use X-ray energies to determine material density via signal attenuation, so sufficient local density variations must be present in the composite to extract fiber orientation information. The $50 \mu\text{m}$ scan resolution used in this work implies that observable variations in local density will not show individual fibers within matrix. Instead, the homogenized mesoscale densities span a range from the pure matrix density to the fiber fraction homogenized density. Without a reference object of known density, the scan data should only be considered as relative density information. An example slice taken from a CT volume shows the relative density data in Fig. 6, where the low-density air is seen as black and the higher densities are various intensities of gray,

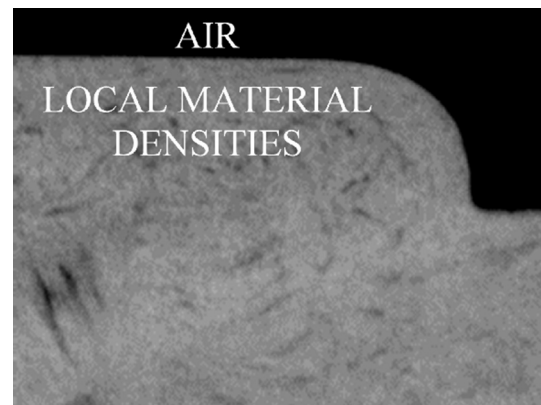


Fig. 6. Example slice of CT volume showing variation in local relative density.

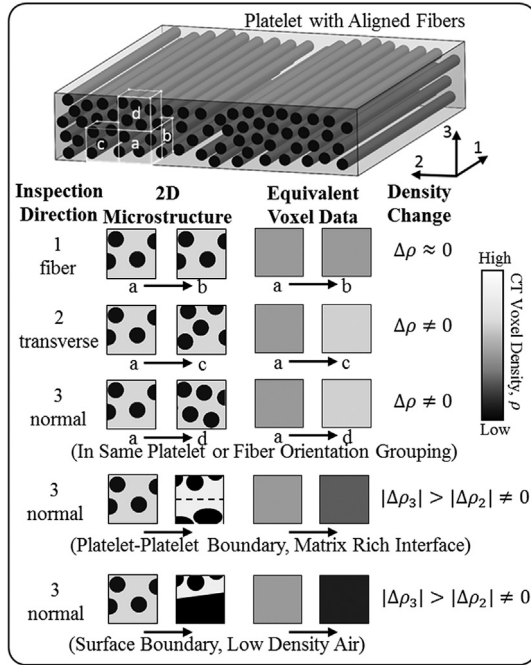


Fig. 7. Density gradients in a single platelet and across platelet boundaries. (For interpretation of the references to colour in this figure legend, the reader is referred to the web version of this article.)

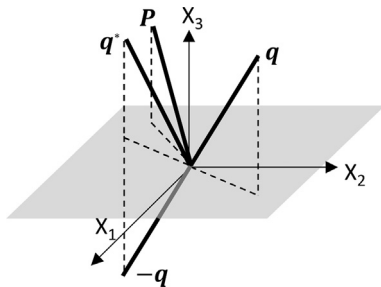


Fig. 8. Possible microscopy fiber vectors, q , compared to CT fiber vector, P .

clearly showing no fiber features.

The CT scans analyzed in this study were taken by North Star Imaging’s scan services department with their X50 scanner. The scan volume is $1264 \times 1264 \times 907$ voxels large in 8-bit format, capturing an object $65 \times 65 \times 45$ mm in size. The geometrically magnified resolution is 18.9 pixels/mm or $53 \mu\text{m}$ edge length voxels, preventing the resolution of 5–7 μm diameter fibers.

3. Analysis methods

3.1. Intact platelet mesostructure enables use of mesoscale CT data

The mesostructure visible in Figs. 3 and 4 prove that the studied PPMC system consists of deformed, but intact, platelets of aligned fibers. The relationship between the changes in the local density field, $\Delta\rho$, and fiber orientation within a platelet is illustrated in Fig. 7. Although the fiber size in the illustrated platelet is exaggerated, the final thickness can be assumed to match the $\sim 100 \mu\text{m}$ observed in specimens, and the inspection regions a–d are sized to match the CT voxel size of this work’s scan resolution. Consider inspecting the local microstructure and corresponding average density along each of the platelet coordinate system axes, 1, 2, and 3. The path parallel to the fiber

direction (1) would be the direction of least density change, as little to no change would occur in the microstructure when moving from region a to region b. The transverse (2) and platelet normal (3) directions exhibit some change in density as the inspection path crosses through different microstructures containing fibers and matrix.

If the inspection regions remain within the example platelet, differentiating between the density changes in the 2- and 3-direction is nearly impossible. However, if neighboring platelets or density features are considered, as in the last two examples of Fig. 7, there is a greater likelihood of differentiating between density changes in the 2 and 3 directions. The direction of greater density change is likely to be normal to the inspected platelet plane, or the 3-direction, where matrix rich platelet interfaces, part exterior boundaries, and variation in platelet fiber volume fraction may be present. The 2-direction would contain changes in density as intra-platelet microstructure variations are encountered. Therefore, assigning the direction of least $|\Delta\rho|$ as the fiber direction in a platelet can be done with confidence, and assigning the direction of greatest $|\Delta\rho|$ as the platelet normal direction is reasonable.

The morphology and CT resolution of this study establish a 1:2 ratio of voxel size to minimum platelet (or fiber bundle) dimension, which serves as a rule of thumb for extension of this work to different geometries or material systems. If the platelets were disaggregated into smaller bundles, then increased CT resolution would be required to determine fiber orientation from the local density gradients from voxel to voxel. Other material forms, such as platelets obtained from a multi-axial, woven material may require reconsideration of the density-direction relationships, but with unidirectional fiber platelets, the above principles relate local density gradients to platelet orientation state and, therefore, fiber orientation.

3.2. CT orientation analysis method

Having established the direction of least density change in a platelet as the fiber direction, a method is now described to determine density changes, or gradients, in the CT scan data. Broadly, the mesoscale density variations in CT scan voxel data are analyzed with 3D Gaussian distribution derivative filters to define local density gradients G_1 , G_2 , and G_3 at each voxel location along the respective global axes directions 1, 2, and 3. Principal analysis of a G_i -based structure tensor yields eigenvectors along the directions of least, most, and median density change. Noise in the measurement data is reduced with a Gaussian smoothing filter prior to assigning the respective eigenvectors to the fiber, platelet normal, and platelet transverse directions. The Mathworks Inc. Matlab 2016a with the Image Processing and Parallel Computing Toolboxes was used for all analysis in this study. Each step is now presented in more detail.

First, an approximate 3D Gaussian distribution, f , over a discrete grid of voxels, with each voxel having centroid coordinates (x_1, x_2, x_3) relative to the central voxel of interest is defined as in Eq. (1). Next, gradient filters, f_{Gi} , are generated by separating components from the gradient of that distribution as presented as Eq. (2).

$$f = e^{-\left(\frac{x_1^2}{2\sigma^2} + \frac{x_2^2}{2\sigma^2} + \frac{x_3^2}{2\sigma^2}\right)} \quad (1)$$

$$\nabla f = (f_{G1}, f_{G2}, f_{G3}) = \left(-\frac{x_1 e^{-\frac{x_1^2+x_2^2+x_3^2}{2\sigma^2}}}{\sigma^2}, -\frac{x_2 e^{-\frac{x_1^2+x_2^2+x_3^2}{2\sigma^2}}}{\sigma^2}, -\frac{x_3 e^{-\frac{x_1^2+x_2^2+x_3^2}{2\sigma^2}}}{\sigma^2} \right) \quad (2)$$

where standard deviation, σ , defines how concentrated the Gaussian distribution is about the filter’s central voxel. Using Matlab’s “imfilter ()” function, with “boundary” = “replicate”, the filters f_{Gi} are convolved about every voxel in the CT scan to find the gradient

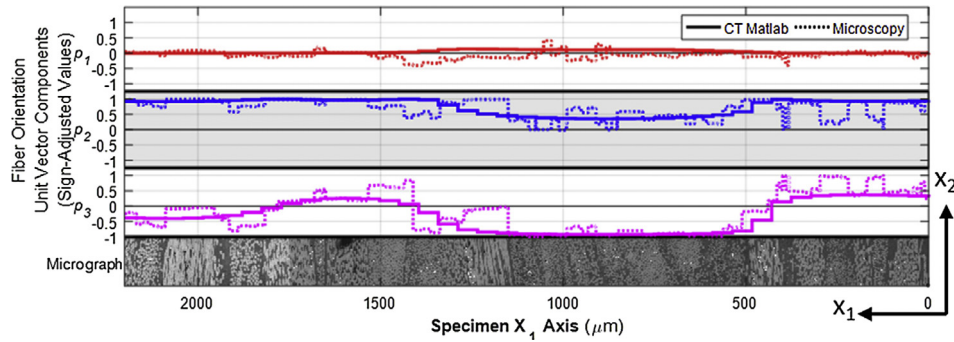


Fig. 9. Best case orientation vector components at line A2 after sign adjustment. (For interpretation of the references to colour in this figure legend, the reader is referred to the web version of this article.)

components, G_i , along each global axis [41]. Gradient components are then used to create the 3×3 structure tensor, S , in Eq. (3) for each voxel [35,42].

$$S = \begin{bmatrix} G_1 G_1 & G_1 G_2 & G_1 G_3 \\ G_1 G_2 & G_2 G_2 & G_2 G_3 \\ G_1 G_3 & G_2 G_3 & G_3 G_3 \end{bmatrix} \quad (3)$$

A Gaussian noise mitigation filter in the form of Eq. (1) is applied to each term of S for the entire data volume. Eigen analysis is performed on the structure tensor to determine the eigenvalues and their eigenvectors associated with the least, median, and greatest density gradients in the CT data. Finally, the eigenvectors of S can be assigned as the fiber, transverse, and platelet-normal directions, respectively, for each voxel. The orientation analysis currently requires less than two hours of parallel processing on a 20-processor HPC node with the “T bracket” scan volume containing 1.5 GB of image slices.

Two effects of filter based image analysis should be considered for this application. The first is the effect of the very large density gradient at the sample-air boundary. This boundary gradient dominates intraspecimen density gradients near the part surface, resulting in fiber orientation measurements strongly aligned with the surface [43]. This effect is reduced slightly in these analyses by replacing the background air density values with a value near the part average density value and is often naturally mitigated when as-molded surfaces have platelets (and fibers) which actually are oriented parallel to the tool surface. Similar boundary effects occur near sufficiently large internal voids and matrix rich regions and should be considered according to the prevalence of such features. The second effect of filter-based analysis regards filter size and the preservation of local detail. Using a filter that is too large for the CT resolution will include too much neighboring data and reduce the clarity of local details. A filter that is too small will not capture the directional density confounded by noise [44].

Gaussian filters are used to mitigate these effects by weighting data closer to the central voxel of inspection. Filter size must be at least $3 \times 3 \times 3$ voxels and contain odd integers to have a central voxel of inspection. Determining the ideal filter size requires consideration of CT scan resolution, platelet dimensions and expected mesostructure type. A heuristic approach yielded comparisons where gradient filter sizes from half a platelet thickness up to three times the platelet thickness produced very similar CT orientation measurement results. The filter sizes used for CT analysis of the “T bracket” geometry’s $53 \mu\text{m}$ scans have a $265 \mu\text{m}$ (5 voxel) edge length to find the gradient components and $1325 \mu\text{m}$ (25 voxel) edge length to mitigate noise in the calculated orientations.

3.3. Orientation comparison methodology

While the second-order orientation tensor, A_{ij} defined by Advani and Tucker, is commonly used to define the fiber orientation distribution in short fiber composites [45], it is not used here because the

platelets have a very high degree of local fiber collimation that can be defined by a single orientation vector. Vectors are decomposed into three components, P_i , at each voxel location within the CT scan and q_i for each fiber ellipse measured in micrographs. Due to the $\mathbf{p} = -\mathbf{p}$ equivalence of a single fiber orientation vector and the $\phi \pm \pi$ ambiguity of microscopy orientation vectors, some data manipulation is required for effective validation. For any microscopy measured orientation vector, \mathbf{q} , an equivalent orientation vector, $-\mathbf{q}$, can be found by multiplying all components by -1 , and an alternate orientation vector, \mathbf{q}^* , can be found by multiplying q_1 and q_2 by -1 as seen in Fig. 8.

The only source available to choose the correct signs of the microscopy orientation vector components is the CT data. The dot product of \mathbf{P} with both \mathbf{q} and \mathbf{q}^* indicates how aligned the vector pairs are. The \mathbf{q} which results in the larger absolute dot product value is more closely aligned with the CT vector \mathbf{P} and will be considered the best case comparison. The \mathbf{q} with a lower dot product is the worst case of the two possible microscopy vectors. The sign adjustment of microscopy data is started by using orientation equivalence to switch between \mathbf{q} and $-\mathbf{q}$ as necessary to match the signs of q_3 to those of P_3 . The alternate $-\mathbf{q}^*$ is created by copying \mathbf{q} and switching the signs of q_1^* and q_2^* . The dot products of \mathbf{q} and \mathbf{q}^* with \mathbf{P} are then calculated and the vector yielding the larger dot product is designated as the best case at each comparison point. Plots of the best and worst case results are shown in Figs. 9 and 10.

With this approach, the CT data retains its measured orientation state and the microscopy data represents each of two possible orientation states. If CT analysis captures orientation magnitude and sign correctly, then the best-case comparison should be considered, otherwise one should look to worst-case comparisons. This choice can be made at each comparison point or for larger regions. Visual comparisons are useful but subjective, so a quantified measure of the success of CT analysis is required. A quantified metric is derived from the second order orientation tensor created from the microscopy and CT measured orientation vectors, \mathbf{q} and \mathbf{P} , at each point using Eq. (4). Although creating an orientation tensor from only two input vectors is not how this tensor is typically used, it provides a means to determine the degree of alignment of the two measurements.

$$A_{ij} = \frac{1}{2}(P_i P_j + q_i q_j) \quad (4)$$

$$A_{ij} \mathbf{v} = \lambda \mathbf{v} \quad (5)$$

Eigen analysis is performed according to Eq. (5) to determine the direction of greatest alignment, $\mathbf{v}_{\lambda_{max}}$, and the relative strength of that alignment, $e_{max} (= \lambda_{max})$, spanning $[0.5, 1]$. That span of e_{max} can alternatively be considered as the angle between the compared CT and microscopy orientation vectors with a respective range of $[90^\circ, 0^\circ]$. Since any one comparison may not represent the CT analysis capability overall, it is useful to consider the distribution of e_{max} values over a full inspection line as in the cumulative distribution function (CDF) plotted for the best- and worst-cases of location A2 in Fig. 11.

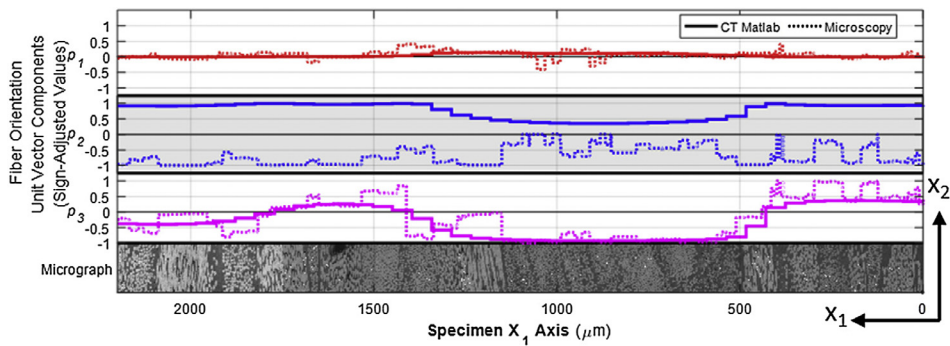


Fig. 10. Worst case orientation vector components at line A2 after sign adjustment. (For interpretation of the references to colour in this figure legend, the reader is referred to the web version of this article.)

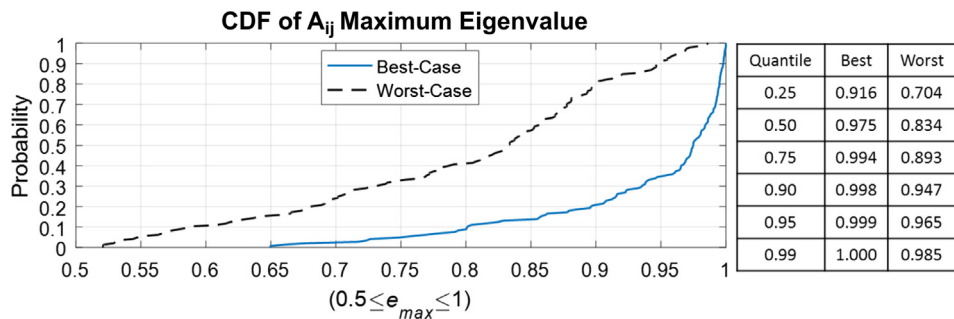


Fig. 11. CDFs at line A2 for best- and worst-case max eigenvalue of orientation tensor A_{ij} . (For interpretation of the references to colour in this figure legend, the reader is referred to the web version of this article.)

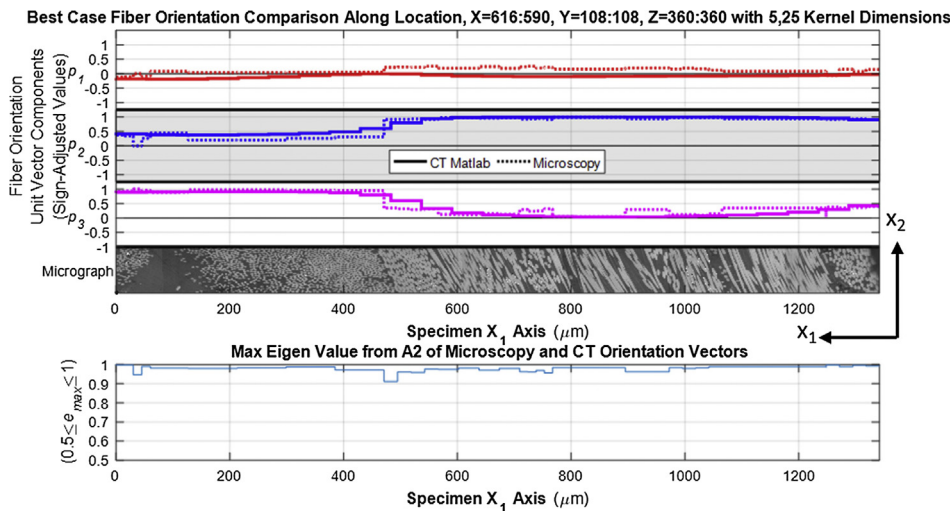


Fig. 12. Location C1 comparison of microscopy and CT data fiber orientation components. (For interpretation of the references to colour in this figure legend, the reader is referred to the web version of this article.)

For the best-case example, the CDF indicates that 50% of the comparisons have a max eigenvalue above 0.97. The comparison of orientation state from CT and microscopy measurement methods can now be performed both qualitatively and quantitatively.

4. CT-Based orientation analysis results validation

CT- and microscopy-measured orientation state are compared using measurements along the nine inspection lines labeled in Fig. 2. The best

correlation occurs where the microstructure contains fewer rapid orientation changes such as that of inspection line, C1, in Fig. 12.

This simple case instills confidence that the CT orientation analysis method is capable of capturing the orientation vector, including the correct vector component signs, very well using the described component sign adjustments. The best- and worst-case data from the large and more typical comparison region, C4, is seen in Fig. 13, where the CT analysis method captures the trends and average magnitudes of fiber orientation components, but not always the discrete platelet

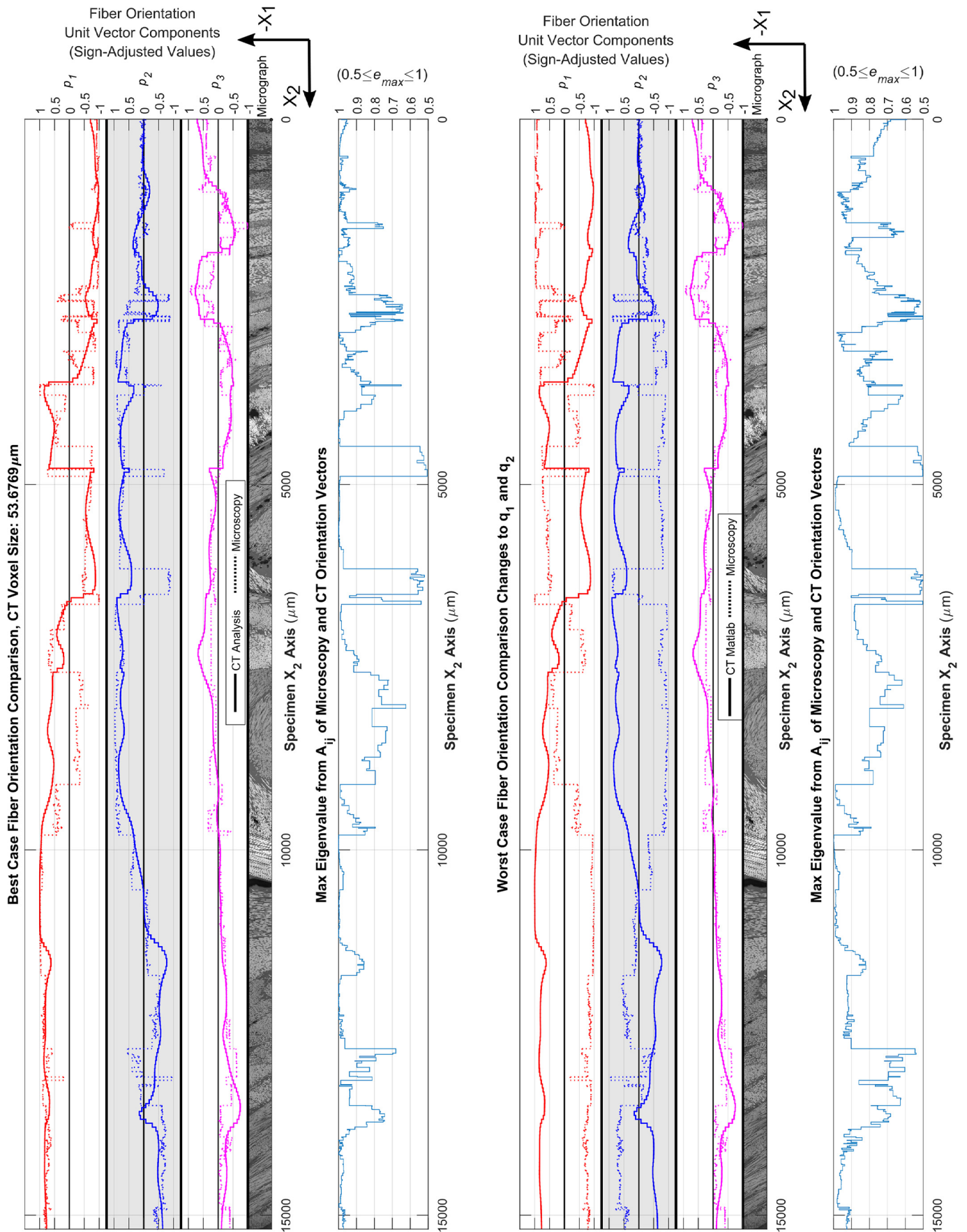


Fig. 13. Location C4 comparison of microscopy and CT data fiber orientation component. (For interpretation of the references to colour in this figure legend, the reader is referred to the web version of this article.)

Table 1
Max eigenvalue CDF quantiles for T bracket best case data comparison.

Individual inspection region quantiles						
	0.25	0.50	0.75	0.90	0.95	0.99
A1	0.872	0.936	0.962	0.992	0.997	0.999
A2	0.916	0.975	0.994	0.998	0.999	1.000
A3	0.773	0.912	0.965	0.990	0.995	0.998
B1	0.946	0.990	0.997	0.999	0.999	1.000
C1	0.968	0.981	0.989	0.996	0.997	0.999
C2	0.863	0.958	0.988	0.995	0.997	0.999
C3	0.887	0.953	0.986	0.993	0.998	0.999
C4	0.907	0.970	0.990	0.997	0.999	1.000
C5	0.957	0.984	0.990	0.997	0.999	1.000

75% of the eigenvalues are better than 0.872. The 0.5 quantile, or median, of the data is recommended as the single value to describe how well CT analysis matched the microscopy baseline. For reference, an e_{max} value of 0.97 corresponds to a 20° angle between the compared vectors and 0.99 corresponds to a 10° angle, the significance of which depends on stress state and local morphology. Region A3 showed the lowest median, which may be a result of an imperfect match of the CT and micrograph comparison locations, or may simply be due to failure of the CT analysis method at this location. To gauge the success of the CT orientation analysis for the entire “T-bracket” geometry inspected, the combined histogram and CDF for all inspection lines is given in Fig. 14.

It is apparent that 50% of the max eigenvalues are greater than 0.963. Although the validation comparisons are performed over relatively small regions, the CT orientation analysis determines the orientation state throughout the entire specimen as shown in Fig. 15.

Only surface orientations are visualized, but the local variability of fiber orientation within each geometry plane and platelet normal vectors parallel to surface normal vectors are indicated. Full orientation state visualization shows that variability is captured at all relevant scales with the CT analysis method.

5. Conclusions

The CT scan orientation analysis outlined is a substantial step toward nondestructive, complete geometry mesostructure characterization and is validated with detailed microscopy. The 50 μm CT scan resolution allows for determination of platelet and fiber orientation fields in this PPMC material system, without the need to distinguish individual fibers. It is the state of fiber collimation and associated physical density gradients within intact platelets that facilitates this unprecedented nondestructive assessment of average local fiber orientation within the entire geometry of interest. This work suggests that CT voxel size should be at least half of the platelet thickness in order to contain sufficient local density gradients for orientation analysis. Comparison methods like the one outlined here may be used on one specimen to ensure validity of the CT analysis method for a specific material, geometry, or scan resolution, and then subsequent CT analyses may be utilized without destructive microscopy. The resulting orientation data is available to map into a finite element model “digital twin” of the scanned part. Many analyses with comparable material and geometry scales can take advantage of this methodology and benefit from a measurement informed orientation state, instead of predictions or assumptions. Examples of such analyses include simulation of experimental performance and validation of manufacturing flow simulation results. While improved image analysis methods and CT scan resolution could yield even better results in future work, this study demonstrates that there is a wealth of data already available to researchers, designers, and material suppliers of prepreg platelet molded composites using current scan technologies.

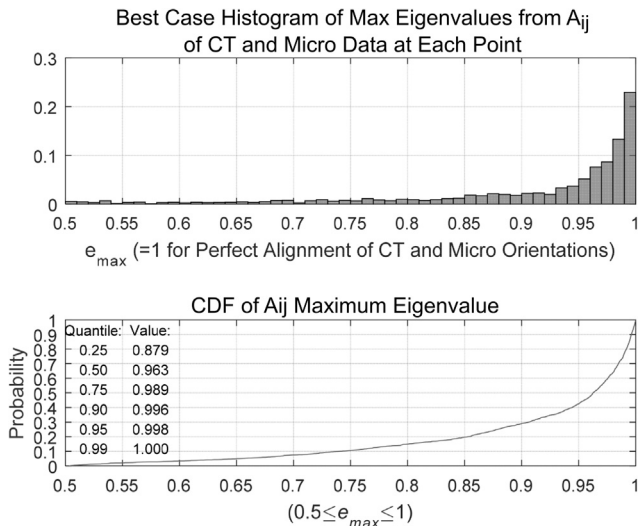


Fig. 14. Histogram and CDF of Max eigenvalue for all orientation vectors in T bracket R5-1. (For interpretation of the references to colour in this figure legend, the reader is referred to the web version of this article.)

boundaries. This is an effect of filter-based image analysis, where measurements utilize a neighborhood of data. Inspection region C4 also contains complex morphology, with a semi-laminate microstructure near either end, and a 3D mixed orientation state in the center seen in Fig. 4. The worst-case plots are also shown in Fig. 13 to acknowledge the possibility of the CT analysis method perfectly mismatching the vector component signs between CT and baseline measurements. However, the visually favorable comparison leads one to assume that the CT analysis is obtaining valid component magnitudes and signs. The quantified error is provided as e_{max} quantile data for the best-case vector comparisons at all nine inspection regions in Table 1.

For inspection region A1, the value at quantile 0.25 is 0.872, meaning 25% of the maximum eigenvalues are worse than 0.872 and

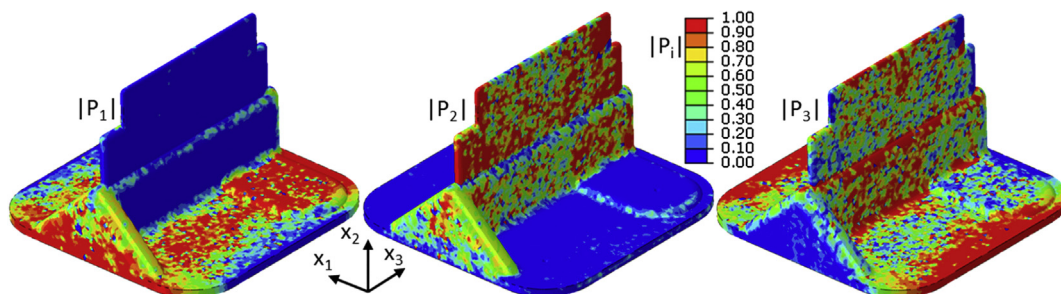


Fig. 15. Orientation vector components from CT analysis for full T-bracket geometry. (For interpretation of the references to colour in this figure legend, the reader is referred to the web version of this article.)

Acknowledgements

The authors wish to thank Boeing Commercial Airplanes for supporting this work.

References

- Chang IY, Pratte JF. LDFTM thermoplastic composites technology. *J Thermoplast Compos Mater* 1991;4:227–52. <https://doi.org/10.1177/089270579100400302>.
- Such M, Ward C, Potter K. Aligned discontinuous fibre composites: a short history. *J Multifunct Compos* 2014;3:155–68. <https://doi.org/10.12783/issn.2168-4286/2/3/4/Such>.
- Turner TA, Warrior NA, Pickering SJ. Development of high value moulding compounds from recycled carbon fibres. *Plast Rubber Compos* 2010;39:151–6. <https://doi.org/10.1179/174328910X12647080902295>.
- Kravchenko SG, Sommer DE, Pipes RB. Uniaxial strength of a composite array of overlaid and aligned prepreg platelets. *Compos Part A Appl Sci Manuf* 2018;109:31–47.
- Visweswaraiyah SB, Selezneva M, Lessard L, Hubert P. Mechanical characterisation and modelling of randomly oriented strand architecture and their hybrids – a general review. *J Reinf Plast Compos* 2018;37:548–80. <https://doi.org/10.1177/0731684418754360>.
- Hayes BS. Introduction—composite materials and optical microscopy. *Opt. Microsc. Fiber-Reinforced Compos*. ASM International; 2010, p. 1–22.
- Bay RS, Tucker CL. Stereological measurement and error estimates for three-dimensional fiber orientation. *Polym Eng Sci* 1992;32:240–53.
- Desplentere F, Lomov SV, Woerdeman DL, Verpoest I, Wevers M, Bogdanovich A. Micro-CT characterization of variability in 3D textile architecture. *Compos Sci Technol* 2005;65:1920–30. <https://doi.org/10.1016/j.compscitech.2005.04.008>.
- Luchoo R, Harper LT, Bond MD, Warrior NA, Dodworth A. Net shape spray deposition for compression moulding of discontinuous fibre composites for high performance applications. *Plast Rubber Compos* 2010;39:216–31. <https://doi.org/10.1179/174328910X12647080902493>.
- Salek H, Denault J. Viscous behavior of resin and flow through the fiber network of carbon. In: Pekk. 9th Int. Conf. Flow Process. Compos. Mater, vol. 9; 2008.
- Landry B, Hubert P. Experimental study of defect formation during processing of randomly-oriented strand carbon/PEEK composites. *Compos Part A Appl Sci Manuf* 2015;77:301–9. <https://doi.org/10.1016/j.compositesa.2015.05.020>.
- Feraboli P, Cleveland T, Ciccu M, Stickler PB, DeOto L. Defect and damage analysis of advanced discontinuous carbon/epoxy composite materials. *Compos Part A Appl Sci Manuf* 2010;41:888–901. <https://doi.org/10.1016/j.compositesa.2010.03.002>.
- Feraboli P, Peitso E, Deleo F, Cleveland T, Stickler PB. Characterization of prepreg-based discontinuous carbon fiber/epoxy systems. *J Reinf Plast Compos* 2009;28:1–24. <https://doi.org/10.1177/0731684408088883>.
- Centea T, Hubert P. Measuring the impregnation of an out-of-autoclave prepreg by micro-CT. *Compos Sci Technol* 2011;71:593–9. <https://doi.org/10.1016/j.compscitech.2010.12.009>.
- Nicoletto G, Riva E, Stocchi A. Mechanical characterization of advanced random discontinuous carbon/epoxy composites. *Mater Today Proc* 2016;3:1079–84. <https://doi.org/10.1016/j.matpr.2016.03.052>.
- Abdul-Aziz A, Saury C, Bui Xuan V, Young PG. On the material characterization of a composite using micro CT image based finite element modeling. *Nondestruct Evalution Heal Monit Diagnostics* 2006;6:176. <https://doi.org/10.1117/12.667766>. 617605-617605–8.
- Stoessel R, Kiefel D, Oster R, Diewel B, Llopard Prieto L. μ -computed tomography for 3d porosity evaluation in carbon fibre reinforced plastics (CFRP). In: *Int Symp Digit Radiol Comput Tomogr*; 2011.
- Weber E, Fernandez M, Wapner P, Hoffman W. Comparison of X-ray micro-tomography measurements of densities and porosity principally to values measured by mercury porosimetry for carbon-carbon composites. *Carbon N Y* 2010;48:2151–8. <https://doi.org/10.1016/j.carbon.2009.11.047>.
- Schilling PJ, Karedla BR, Tatiparthi AK, Verges MA, Herrington PD. X-ray computed microtomography of internal damage in fiber reinforced polymer matrix composites. *Compos Sci Technol* 2005;65:2071–8. <https://doi.org/10.1016/j.compscitech.2005.05.014>.
- Tan KT, Watanabe N, Iwahori Y. X-ray radiography and micro-computed tomography examination of damage characteristics in stitched composites subjected to impact loading. *Compos Part B Eng* 2011;42:874–84. <https://doi.org/10.1016/j.compositesb.2011.01.011>.
- Robb K, Wirjadi O, Schladitz K. Fiber orientation estimation from 3D image data: practical algorithms, visualization, and interpretation. In: 7th Int. Conf. Hybrid Intell. Syst. (HIS 2007); 2007. p. 320–5. <http://doi.org/10.1109/HIS.2007.26>.
- Shen H, Nutt S, Hull D. Direct observation and measurement of fiber architecture in short fiber-polymer composite foam through micro-CT imaging. *Compos Sci Technol* 2004;64:2113–20. <https://doi.org/10.1016/j.compscitech.2004.03.003>.
- Fliegner S, Luke M, Gumbsch P. 3D microstructure modeling of long fiber reinforced thermoplastics. *Compos Sci Technol* 2014;104:136–45. <https://doi.org/10.1016/j.compscitech.2014.09.009>.
- Gandhi U, Sebastian DB, Kunc V, Song Y. Method to measure orientation of discontinuous fiber embedded in the polymer matrix from computerized tomography scan data. *J Thermoplast Compos Mater* 2015. <https://doi.org/10.1177/0892705715584411>.
- Czabaj MW, Riccio ML, Whitacre WW. Numerical reconstruction of graphite/epoxy composite microstructure based on sub-micron resolution X-ray computed tomography. *Compos Sci Technol* 2014;105:174–82. <https://doi.org/10.1016/j.compscitech.2014.10.017>.
- Scott AE, Mavrogordato M, Wright P, Sinclair I, Spearing SM. In situ fibre fracture measurement in carbon-epoxy laminates using high resolution computed tomography. *Compos Sci Technol* 2011;71:1471–7. <https://doi.org/10.1016/j.compscitech.2011.06.004>.
- Moffat AJ, Wright P, Helfen L, Baumbach T, Johnson G, Spearing SM, et al. In situ synchrotron computed laminography of damage in carbon fibre-epoxy [90/0]s laminates. *Scr Mater* 2010;62:97–100. <https://doi.org/10.1016/j.scriptamat.2009.09.027>.
- Whitacre WW. Automated 3D digital reconstruction of fiber reinforced polymer composites. In: *AIAA Guid. Navig. Control Conf., Kissimmee, FL*; 2015. p. 1–18. <http://doi.org/10.2514/6.2015-0342>.
- Whitacre WW, Wood RJ, Czabaj MW. Extension of automated 3D digital reconstruction to multi-directional fiber reinforced composite microstructures. In: 57th AIAA/ASCE/AHS/ASC Struct. Struct. Dyn. Mater. Conf.; 2016. p. 1–9. <http://doi.org/10.2514/6.2016-1233>.
- Maier D, Dierig T, Reinhart C, Günther T. Analysis of woven fabrics and fiber composite material aerospace parts using industrial CT data. In: 5th Int. Symp. NDT Aerosp., Singapore; 2013. p. 13–5.
- Goris S, Osswald TA. Process-induced fiber matrix separation in long fiber-reinforced thermoplastics. *Compos Part A Appl Sci Manuf* 2018;105:321–33. <https://doi.org/10.1016/j.compositesa.2017.11.024>.
- Krumm M, Sauerwein C, Hämmerle V, Oster R, Diewel B, Sindel M. Capabilities and application of specialized computed tomography methods for the determination of characteristic material properties of fiber composite components. *Ind. Comput. Tomogr., Wels, Austria*; 2012. p. 41–8.
- Simon M, Sauerwein C, Tiseanu I. Extended 3D CT method for the inspection of large components. In: 16th World Conf. Non-Destructive Test., Montreal; 2004.
- Leblanc D, Landry B, Levy A, Hubert P, Roy S, Yousefpour A. Compression moulding of complex parts using randomly-oriented strands thermoplastic composites. *Sampe* 2014;2014:14.
- Krause M, Hausherr JM, Burgeth B, Herrmann C, Krenkel W. Determination of the fibre orientation in composites using the structure tensor and local X-ray transform. *J Mater Sci* 2010;45:888–96. <https://doi.org/10.1007/s10853-009-4016-4>.
- Han JH, Khawaja A, Kilic MH, Ingram K. Identification of fiber orientation prediction error by moldflow on compression molded discontinuous long fiber composites using computed tomography X-ray. In: *CAMX Conf. Proc.*; 2015.
- Han JH, Ph D. Experimental validation of fiber orientation prediction by flow simulation on compression molded discontinuous long-fiber composites using computed tomography imaging. In: *CAMX Conf. Proc.*; 2016.
- Davidson NC, Clarke AR, Archenhold G. Large-area, high-resolution image analysis of composite materials. *J Microsc* 1997;185:233–42. <https://doi.org/10.1046/j.1365-2818.1997.1560712.x>.
- Vincent M, Giroud T, Clarke A, Eberhardt C. Description and modeling of fiber orientation in injection molding of fiber reinforced thermoplastics. *Polymer (Guildf)* 2005;46:6719–25. <https://doi.org/10.1016/j.polymer.2005.05.026>.
- Schindelin J, Arganda-Carreras I, Frise E. Fiji: an open-source platform for biological-image analysis. *Nat Methods* 2012;9:676–82.
- Ohser J, Schladitz K. 3D images of materials structures: processing and analysis. Wiley-VCH 2009. <https://doi.org/10.1002/9783527628308>.
- Haußecker H, Jähne B. A tensor approach for local structure analysis in multi-dimensional images. *3D Image Anal. Synth., Sankt Augustin*; 1996. p. 171–8.
- Ge Y, Cheng Q. Boundary effect reduction in image filtering. *ICGST Int J Graph Vis Image Process GVIP* 2007;7:17–25.
- Ahmed ESA, Elatif REA, Alser ZT. Median filter performance based on different window sizes for salt and pepper noise removal in gray and RGB images. *Int J Signal Process Image Process Pattern Recognit* 2015;8:343–52. <https://doi.org/10.14257/ijsp.2015.8.10.34>.
- Advani SG, Tucker CL. The use of tensors to describe and predict fiber orientation in short fiber composites. *J Rheol (N Y N Y)* 1987;31:751. <https://doi.org/10.1122/1.549945>.